Journal of Materials Chemistry C

ROYAL SOCIETY OF CHEMISTRY

PAPER

View Article Online
View Journal | View Issue

Cite this: J. Mater. Chem. C, 2023, 11, 8243

Fluorinated- and non-fluorinated-diarylamine-Zn(II) and Cu(II) phthalocyanines as symmetrical *vs.* asymmetrical hole selective materials†

Adrián Hernández, ‡[a] Naveen Harindu Hemasiri, ‡[b] Samrana Kazim, [bc] Javier Ortiz, [a] Shahzada Ahmad *[bc] and Ángela Sastre-Santos *[a]

Received 20th January 2023,
Accepted 25th March 2023

DOI: 10.1039/d3tc00254c

rsc.li/materials-c

Four symmetrically substituted and four asymmetrically substituted fluorinated and non-fluorinated-diarylamine CuPcs and ZnPcs have been designed and utilized as hole transporting materials in perovskite solar cells in a planar n–i–p structure. We established the correlation between the electronic structure, charge mobility parameters, core metal, and substituents in metal phthalocyanines. The fluorinated asymmetrically substituted undoped **ZnPc-6** yielded the best power conversion efficiency of 15.40% with an open-circuit voltage (V_{oc}) of 1016.1 mV, a short-circuit current density (J_{sc}) of 21.27 mA cm^{-2}, and a fill factor (FF) of 71.25%, followed by the non-fluorinated asymmetrically substituted **ZnPc-5** with 14.36%. In the case of symmetrical CuPcs, the best performance was measured using non-fluorinated **CuPc-3** and fluorinated **CuPc-4** gave 11.53% and 10.90% of PCEs, respectively. Importantly, the devices with MPcs showed improved stability under multi-stress conditions.

10th Anniversary Statement

We would like to congratulate *Journal of Material Chemistry* on its 10th anniversary and will like to thank the journal for letting us publish four different reviews and two full articles during this decade. We are organic chemists and *J. Mater. Chem.* has helped us a lot to disseminate our work with different reviews such as components in bulk heterojunctions, dye sensitized solar cells and single molecules in photovoltaic technologies. This article highlights the importance of phthalocyanines, as components of perovskite solar cells acting as hole transporting materials. Our future directions focus on the search of new materials improving their semiconductor capabilities as well as their self-assembly organization that could help achieve a better performance in photovoltaic devices.

1. Introduction

The preliminary work of perovskite solar cells (PSCs) can be traced back to Miyasaka *et al.* using perovskite as a dye in dye-sensitized solar cells measuring 3.8% efficiency.[1] Today, the improvement is remarkable with a 25.7% efficiency.[2] This development is due to the unmatched properties of halide perovskites such as a broad absorption spectral range, a long carrier diffusion length, ambipolar charge transport, and solution processability.[3–5] These properties, along with ease of fabrication and low cost due to less material usage,[6] make PSCs a promising technology on the way to decreasing carbon emissions.

On the other hand, the development of low-cost, efficient, and stable hole transporting materials (HTMs) is a prerequisite for the commercialization of PSCs. HTMs provide electron blocking and charge extraction at a perovskite/HTM interface, as well as transport holes to the electrode. Furthermore, in an n–i–p configuration, a HTM can increase the stability of a device by protecting the perovskite layer against humidity and oxygen.[7]

2,2′,7,7′-*tetrakis*-(*N*,*N*-di-*p*-methoxyphenylamine)-9,9′-spirobifluorene (Spiro-OMeTAD) is the HTM used par excellence in n–i–p type PSCs, but possesses low hole mobility in its pristine form.[8,9] To improve its electrical properties, dopants and additives such as lithium bis(trifluoromethanesulfonyl)imide (Li-TFSI), a cobalt complex, and 4-*tert*-butylpyridine (*t*-BP) have been commonly used. However, doping also accelerates the degradation of perovskite layers due to the hygroscopic nature of dopants and additives that decrease the long-term

[a] Área de Química Orgánica, Instituto de Bioingeniería, Universidad Miguel Hernández, Avda. Universidad S/N, 03202, Elche, Spain. E-mail: asastre@umh.es
[b] BCMaterials, Basque Center for Materials, Applications, and Nanostructures, UPV/EHU Science Park, 48940, Leioa, Spain. E-mail: shahzada.ahmad@bcmaterials.net
[c] IKERBASQUE, Basque Foundation for Science, Bilbao, 48009, Spain

† Electronic supplementary information (ESI) available. See DOI: https://doi.org/10.1039/d3tc00254c

‡ Equal contribution

stability of PSCs.[10,11] It is of high research interest to develop dopant-free HTMs that can overcome the limitations of doped HTMs and are UV stable.[12]

Phthalocyanines are synthetic analogs of porphyrins that stand out for their effective photochemical and electrochemical stability.[13] Metal phthalocyanines (MPcs) have recently been used as HTMs in PSCs.[14,15] Earlier, we reported ZnPc dimers as HTMs, which gave good performance and stability without the addition of dopants, owing to their extended electron delocalization and high charge mobility.[16–18] On the other hand, the use of various metals, along with different peripheral and nonperipheral substituents, can modify the optical and electrical properties of MPcs and improve their solubility in conventional solvents.[19] Recently, NiPc substituted with four methoxyethoxy groups has been reported and the devices also exhibited good moisture, thermal, and light stabilities.[20]

On the other hand, arylamine groups, particularly triphenylamine (TPA) or diphenylamine (DPA) based compounds, have been extensively utilized as small-molecule HTMs in PSCs due to their excellent hole-transporting properties, electron–donor ability, high stability, and solubility.[21] Reports on employing these groups as substituents for MPcs as HTMs are scarce and not well exploited. Nazeeruddin and co-workers reported PSCs with a PCE of 11.75% using doped DPA-substituted ZnPc.[22] Similarly, a ZnPc having four peripheral TPA substituents in PSCs achieved a PCE of 5.6%.[23] The photovoltaic performance of PSCs fabricated with doped OMe–DPA–CuPc (16.73%) and OMe–TPA–CuPc (19.67%) was compared, featuring four bis-(4-methoxyphenyl)amino substituents and four *N,N*-bis(4-methoxyphenyl)benzenamino substituents, respectively.[24] Zn(II) and Cu(II) Pcs with arylamine groups having different alkoxy chains were compared and a PCE of 20.18% for their best-doped MPc was measured.[25] Our group studied arylamine-based substituents in MPcs such as ZnTTPc,[26] ZnPcTTPA, and CuPcTTPA[27] as undoped HTMs in PSCs. Recently, it was found that the presence of fluorine atoms in phthalocyanines can up-shift the energy level of the highest occupied molecular orbital (HOMO) and lowest unoccupied molecular orbital (LUMO) and enhance interfacial charge transfer, this also improves the stability of a device due to the increased hydrophobic character that prevents the entry of moisture.[28] Moreover, efforts to establish a direct relationship between the nature of a metal ion and the phthalocyanine substituents with electronic properties to optimize photovoltaic devices have not been reported. Moreover, in comparison, asymmetric structures tend to have excellent solubility and thermal stability and hold potential for application as HTMs. Yet, asymmetric HTMs have been relatively less studied to date compared to their symmetric counterparts.[29]

In this work, we designed symmetrical and unsymmetrical substituted phthalocyanines to study the effect of the inclusion of fluorine atoms in the arylamino substituents and the variation of the central metal ion on the conductivity and hole mobility and their integration as HTMs in PSCs.

Symmetrical phthalocyanines, **ZnPc-1** and **CuPc-3,** have four diphenylamine (DPA), while **ZnPc-2** and **CuPc-4** consist of four fluorinated diphenylamine (FDPA) substituents, respectively. In the case of asymmetric ones, **ZnPc-5** and **CuPc-7** contain

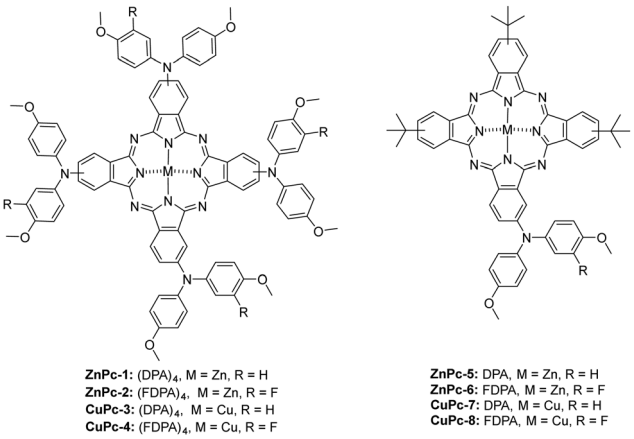

Fig. 1 Molecular structure of **ZnPc-1**, **ZnPc-2**, **CuPc-3**, **CuPc-4**, **ZnPc-5**, **ZnPc-6**, **CuPc-7**, and **CuPc-8**.

one DPA unit and three *tert*-butyl groups while **ZnPc-6** and **CuPc-8**, are substituted with one fluorinated DPA unit and three *tert*-butyl groups, which have worked well in previously reported PSCs. Using both families, we have prepared zinc and copper analogs (Fig. 1).

2. Results and discussion

Synthesis of MPCs

Phthalonitriles **1** and **2** were synthesized by a high-yield palladium-catalyzed substitution of 4-iodophthalonitrile with the corresponding secondary amine (Fig. 2). Phthalonitriles **1** and **2** were characterized by ^{1}H-NMR and ^{13}C-NMR spectroscopies. Synthesis of symmetrical MPcs was carried out by cyclotetramerization of the corresponding phthalonitrile (**1** or **2**) and $Zn(OAc)_2$ or $CuCl_2$ using DMAE as a solvent and DBN as

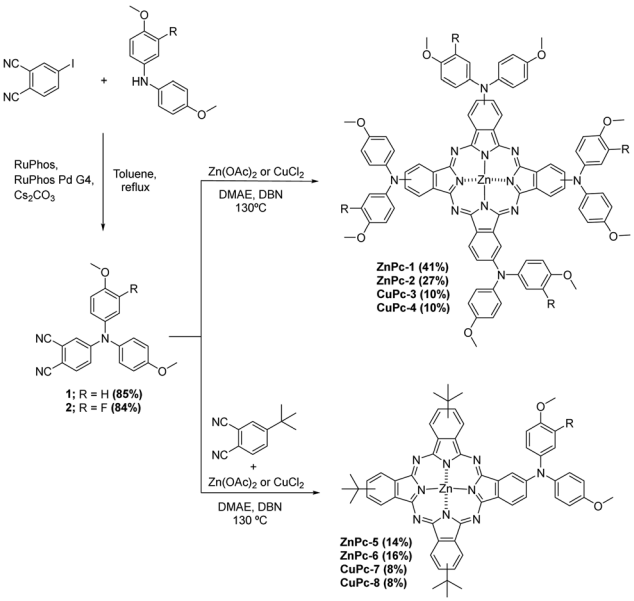

Fig. 2 Synthetic route of phthalonitriles and the MPcs.

catalyst. After purification by silica gel column chromatography, **ZnPc-1**, **ZnPc-2**, **CuPc-3**, and **CuPc-4** were obtained with a yield of 41%, 27%, 10%, and 10%, respectively. For the synthesis of asymmetrical MPcs, a statistical cyclotetramerization between 4-*tert*-butylphthalonitrile and the appropriate phthalonitrile (**1** or **2**) and zinc acetate or Cu(II) chloride was performed. After careful purification by silica gel column chromatography, **ZnPc-5**, **ZnPc-6**, **CuPc-7**, and **CuPc-8** were obtained with 14%, 16%, 8%, and 8% yield, respectively. All MPcs were obtained as mixtures of regioisomers (Fig. 2). The yields obtained for copper phthalocyanines are lower because their purification is more difficult, in addition to the fact that copper exerts a worse template effect than zinc in the cyclotetramerization reaction. Asymmetrical MPcs yields are the lowest because all the possible statistical phthalocyanines are formed in the reaction and they must be carefully separated. All the new MPcs are highly soluble in organic solvents such as $CHCl_3$ and THF; however, they are not soluble in MeOH and hexane. The synthesized MPcs are quite stable and have melting temperatures typically above 300 °C without decomposition.

The ^{1}H-NMR spectra of ZnPcs in THF-d_8 showed well-defined aromatic and aliphatic signals. The **ZnPc-1** spectrum shows six signals from the isoindole units between 9.2–8.6 and 7.6 ppm; regarding the aromatic chain, we can appreciate two multiplets from the phenyl groups between 7.4–7.0 ppm and a singlet from the methoxy groups at 3.86 ppm. The **ZnPc-2** spectrum is not as well resolved as the other ZnPcs but we can still appreciate the peaks from the isoindole units a little shifted downfield compared with **ZnPc-1**. Furthermore, we observe a new peak at 7.2 ppm due to the loss of symmetry on the phenyl group by the fluorine atom (Fig. 3 and ESI†).

From the **ZnPc-5** spectrum, the three isoindole units with the *tert*-butyl groups show three new signals between 9.5–9.2 and 8.3 ppm, a signal at 1.8 ppm from the *tert*-butyl group, and the peaks from the fourth isoindole unit are shifted downfield compared with **ZnPc-1**. The **ZnPc-6** spectrum is equal to the one of **ZnPc-5**, except for the loss of symmetry on the phenyl group by the fluorine atom with a new peak at 7.2 ppm as occurs with **ZnPc-2**. (Fig. 3 and ESI†).

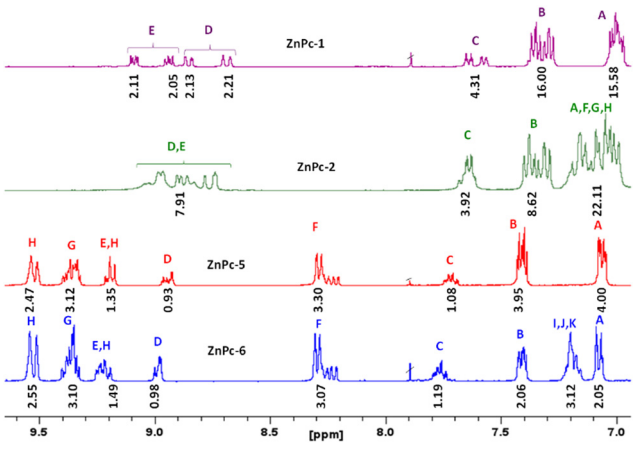

Fig. 3 ^{1}H-NMR spectra of ZnPcs in THF-d_8.

Characterization by NMR experiments could not be achieved for CuPcs due to the paramagnetic character of copper (II). Nevertheless, all MPcs were characterized using Fourier transform infrared spectroscopy (FT-IR), high-resolution-matrix-assisted laser desorption ionization time-of-flight mass spectrometry (HR-MALDI-TOF), and UV-vis absorption spectroscopy measurements.

We performed the FT-IR spectra using a KBr pellet (ESI†). From the different signals of the Pcs, highlight the peaks at 1263, 1256, 1263, and 1258 cm^{-1} of **ZnPc-2**, **ZnPc-6**, **CuPc-4**, and **CuPc-8,** respectively, corresponding to the C–F stretching of the fluorine atoms.

Electro-optical and physical properties

The UV-vis absorption spectra measured in DMF solvent show the commonly known Soret and Q bands, at around 350 nm and 600–780 nm, respectively. In addition, we can observe a charge transfer band at 500 nm for the symmetrical MPcs.

The Q bands of the MPcs are shown in Table 1. An increase in the molar extinction coefficient and a small hypsochromic shift are observed in phthalocyanines substituted with fluorinated arylamines. While, in the case of asymmetric Pcs, a large hypsochromic shift and a minor increase in the molar extinction coefficient can be seen as compared to their symmetric counterparts. Furthermore, we noted a decrease in the molar extinction coefficient when the metal ion is changed from Zn(II) to Cu(II) as well as a hypsochromic shift, which is higher in the symmetrical Pcs (Fig. 4a and b).

The electrochemical characterization was performed by cyclic voltammetry in dry DMF solvent and ferrocene was used as an external standard. The highest occupied molecular orbital energy levels (E_{HOMO}) were calculated from the equation: $E_{HOMO} = -4.8 - E_{Ox1}$, where E_{Ox1} is the first oxidation potential. The LUMO energy level (E_{LUMO}) was calculated by adding the optical band gap to the E_{HOMO} value. CuPcs showed lower E_{HOMO} levels compared to ZnPcs. A similar effect can be observed in the asymmetrically substituted Pcs, and with the addition of fluorine atoms to the Pcs. Symmetrical Pcs presented a smaller band gap. Nevertheless, they showed adequate E_{HOMO} energy values for hole extraction from the perovskite.

In a similar fashion, E_{LUMO} energy is appropriate to prevent the flow of the photogenerated electron and will avoid recombination at the perovskite-HTM interface.

In the absorbance spectra of the phthalocyanines deposited as a thin film, a general broadening of the bands and the

Table 1 Electro-optical properties of the different MPcs

MPc	Q band	$E_{g\ optical}$	E_{Ox1}	E_{Ox2}	E_{HOMO}	E_{LUMO}
ZnPc-1	733	1.68	0.00	0.33	−4.80	−3.12
ZnPc-2	726	1.69	0.04	0.40	−4.84	−3.15
CuPc-3	749	1.57	0.07	0.49	−4.87	−3.30
CuPc-4	740	1.59	0.15	0.56	−4.95	−3.36
ZnPc-5	692	1.77	0.12	0.48	−4.92	−3.15
ZnPc-6	690	1.78	0.14	0.56	−4.94	−3.16
CuPc-7	697	1.70	0.18	0.51	−4.98	−3.28
CuPc-8	694	1.71	0.29	0.61	−5.09	−3.38

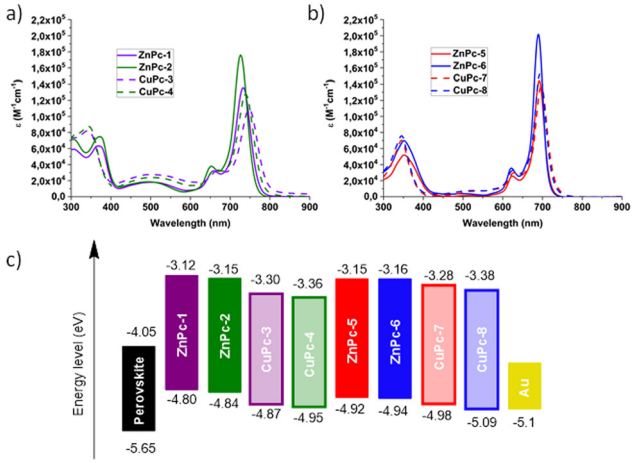

Fig. 4 UV-vis absorption spectra of MPcs in solution, (a) symmetric MPcs, (b) asymmetric MPcs, and (c) energy level diagram for the MPcs.

splitting of the Q-band can be appreciated, phenomena attributable to the formation of aggregates. The shorter wavelength peak is due to aggregate species and face-to-face stacking of the molecules, while the peak at longer wavelengths is due to monomeric species. This phenomenon can be noted in the case of the phthalocyanines **CuPc-4**, **ZnPc-5**, and **ZnPc-6** (Fig. 5a). In the perovskite/HTM absorption spectra deposited as a thin film, the contribution of the phthalocyanines to the absorption is observed, as expected, at wavelengths between 700 and 800 nm (Fig. 5b).

Photovoltaic performance of PSCs with MPcs as HTMs

PSCs were fabricated with a planar n–i–p structure of fluorine-doped tin oxide (FTO)/bl-TiO_2/SnO_2/perovskite/MPc/Au using different MPcs as HTMs to investigate the effect of the core metal and different substitutions on their photovoltaic performance (Fig. 6a). Owing to the superior optical absorption and higher stability, a triple-cation perovskite, with the chemical formula of $Cs_{0.1}(FA_{0.9}MA_{0.1})_{0.9}Pb(I_{0.9}Br_{0.1})_3$ was deposited by antisolvent-assisted one step method.[30] The concentration of each HTM was maintained at 10 mM for device fabrication. All layers in the device were deposited by the solution process except the gold anode, which is thermally evaporated. The current density–voltage (J–V) curves measured under the reverse scan of the PSCs based on symmetric (Fig. 6b) and asymmetric (Fig. 6c) MPcs are presented. The corresponding photovoltaic parameters derived from the graph are summarized in Table 2.

The reference device using undoped PTAA as HTM gave a PCE of 15.53% (Fig. S44, ESI†). Notably, among all the MPc-HTMs investigated here, the best PV performances were measured from Zn-based asymmetric Pcs, which are on par with the PTAA-based devices. In particular, the **ZnPc-6** HTM yielded the maximum PCE of 15.40% with an open-circuit voltage (V_{oc}) of 1016.11 mV, a short-circuit current density (J_{sc}) of 21.27 mA cm^{-2}, and a fill factor (FF) of 71.25%, followed by **ZnPc-5** with 14.36% of PCE. To note here, the measured FF from these fluorinated substituted asymmetrical Pcs is highest compared to other Pcs.

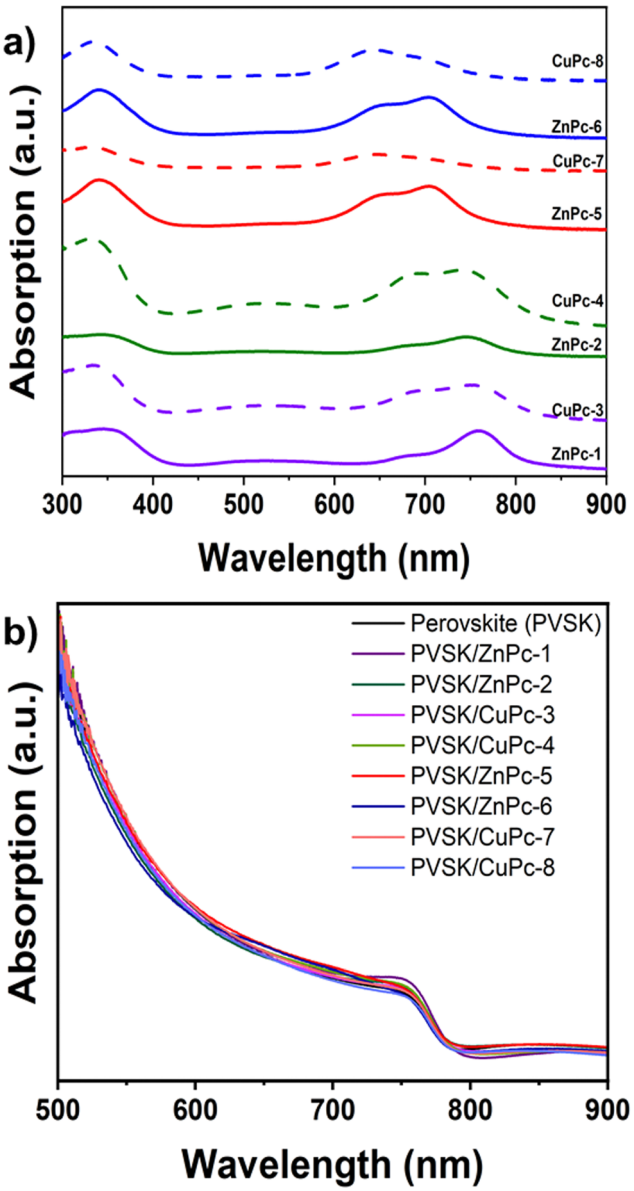

Fig. 5 UV-vis absorption spectra in thin films of (a) MPcs, (b) perovskite with MPcs.

Similarly, from the symmetrical Pc category, **ZnPc-2** gave a PCE of 12.66% with a V_{oc} of 930.72 mV, 20.58 J_{sc} of 20.6 mA cm^{-2}, and a FF of 66.06%. Contrary to Zn based Pcs, in case of CuPcs, the best efficiencies were noted from the symmetrical Pcs, in which **CuPc-3** and **CuPc-4** gave 11.53% and 10.90% of PCEs, respectively. A similar trend can be found from the statistical distribution of the PCE of different MPc-HTMs (Fig. 6d and Table S1, ESI†). Moreover, the measured J_{sc} from the J–V curve decreases when the coordination metal Zn(II) is switched out for Cu(II). In general, the deeper HOMO state of the HTM relative to the perovskite's valence band maximum (VBM) (−5.65 eV) would enable a rational energy alignment, which in turn will facilitate charge extraction; subsequently, the smaller the energy barrier between the perovskite and the HTL, the lower the recombination and minimum voltage (V_{oc}) deficit will be.[31,32] This behavior can be deduced

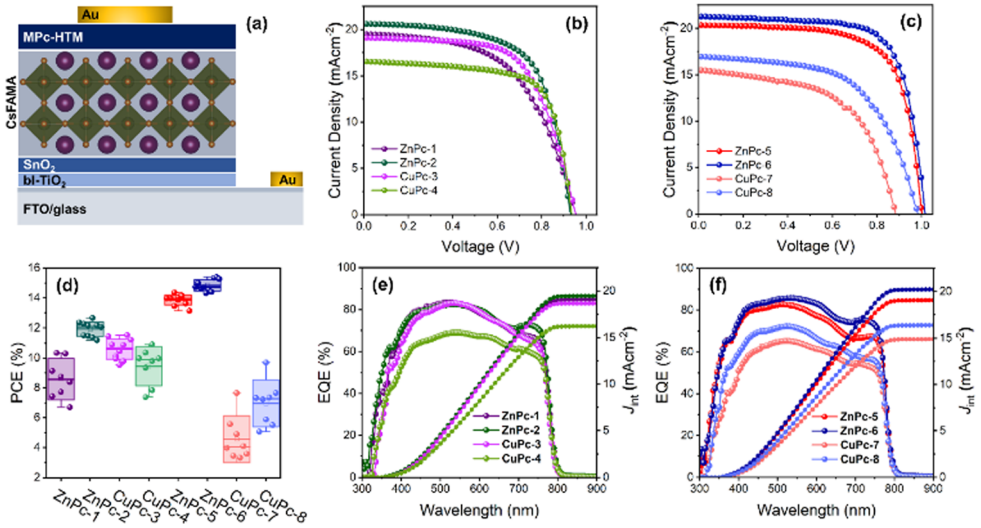

Fig. 6 Proposed device architecture: fluorine-doped tin oxide (FTO)/bl-TiO_2/SnO_2/perovskite/MPc/Au (a), *J–V* curves of the device using (b) symmetric MPcs and (c) asymmetric MPcs, (d) statistical PCE of PSCs with different MPc-HTMs, corresponding IPCE and integrated current density (J_{int}) of the device with (e) symmetric MPcs and, (f) asymmetric MPcs.

Table 2 Performance summary of devices with different MPcs as HTMs

HTM	Scan	V_{OC} (mV)	J_{sc} (mA cm^{-2})	FF (%)	PCE (%)	R_s (Ω)	R_{sh} (kΩ)
ZnPc-1	RS	954.9	19.48	55.57	10.34	136.89	7.9
	FS	871.4	19.29	30.37	5.11	240.89	0.6
ZnPc-2	RS	930.7	20.58	66.06	12.66	72.10	15.5
	FS	932.2	20.48	61.36	11.71	100.42	12.0
CuPc-3	RS	953.5	19.08	63.35	11.53	109.29	17.6
	FS	946.4	19.12	47.52	8.59	141.87	1.1
CuPc-4	RS	935.5	16.54	70.46	10.90	55.18	9.7
	FS	917.4	16.49	61.35	9.28	127.73	2.8
ZnPc-5	RS	1000.9	20.33	70.59	14.36	57.93	20.7
	FS	999.6	20.21	67.15	13.57	72.79	19.7
ZnPc-6	RS	1016.1	21.27	71.25	15.40	53.50	24.0
	FS	1013.3	21.18	68.77	14.76	63.43	20.1
CuPc-7	RS	884.9	15.49	55.82	7.65	122.75	4.1
	FS	848.9	14.69	39.59	4.94	190.09	0.3
CuPc-8	RS	982.8	16.96	58.17	9.69	124.34	6.7
	FS	955.3	16.28	57.48	8.94	129.19	3.2
PTAA	RS	1031.7	20.55	73.28	15.53	52.15	17.3
	FS	1023.0	20.47	73.90	15.48	53.60	10.0

from ZnPcs, where the deeper HOMO levels associated with **ZnPc-5** and **ZnPc-6** close to the VBM of the triple-cation perovskite facilitate a higher V_{oc} when compared with a shallow HOMO level associated with **ZnPc-1** and **ZnPc-2**. However, the V_{oc} variation cannot be correlated to the HOMO state position of the Cu-based Pc series. This is per similar behavior of V_{oc} variation from Zn- and Cu-based MPcs irrespective of their HOMO state position.[33] Arguably, our finding suggests that the PCE not only depends on the symmetrical nature of the side chain of the MPc but also the metal species attached to it.

The external quantum efficiency (EQE) spectra of the symmetrical (Fig. 6e) and asymmetrical (Fig. 6f) MPc-based PSCs were recorded to examine the photoresponsivity. The integrated current density values are calculated as 19.05, 19.46, 18.65, 16.19, 19.0, 20.23, 14.88, and 16.36 mA cm^{-2} for **ZnPc-1**, **ZnPc-2**, **CuPc-3**, **CuPc-4**, **ZnPc-5**, **ZnPc-6**, **CuPc-7**, and **CuPc-8**, respectively, which are consistent with the tendency of J_{sc} obtained from *J–V* curves. All MPc-HTMs exhibit a significant reduction in EQE at wavelengths over 600 nm, which is following the strong absorption band of MPcs in the range of 600–800 nm. The amount of current produced by the second pass of reflected light from the gold electrode can be dramatically reduced by this absorption corresponding to MPcs. Although all MPcs have B-band absorption in a lower wavelength region below 400 nm, the aforementioned effect cannot be seen for high-energy photons since the perovskite layer has a higher absorption coefficient at a shorter wavelength.

The reverse and forward scan *J–V* profiles were recorded to uncover the hysteresis behavior of each MPc-HTM (Fig. S45 and S46, ESI†) and the hysteresis indices (HIs) are summarized in Table S1 (ESI†). We noted reduced hysteresis from the PSCs incorporating **ZnPc-5** and **ZnPc-6**, though the high efficiencies were noted from **ZnPc-2** and **CuPc-3** in the symmetric MPc group they also feature considerable hysteresis. Table 2 summarizes the series resistance (R_s) and shunt resistance (R_{sh}), which were extracted from the slope at V_{oc} and J_{sc}, respectively, from the corresponding *J–V* curve. The device made with **ZnPc-5** and **ZnPc-6** exhibits a lower R_s and a higher R_{sh}, both of which boost the FF and V_{oc} of the PSC by reducing interfacial charge losses and non-radiative charge recombination in the device.[30] Additionally, the stabilized J_{sc} (Fig. 7a) was measured for the initial 300 s for PSCs with **ZnPc-2**, **CuPc-3**, **ZnPc-5**, and **ZnPc-6** as HTMs at their maximum power point (MPP) under ambient conditions (40–60% at 28 °C), which is in agreement with J_{sc} measured from their *J–V* curves. Overall, the best PV performances were observed from **ZnPc-6** > **ZnPc-5** > **ZnPc-2**. We also studied the potential of these MPcs as HTL in inverted (*p-i-n*) PSC with an architect of FTO/MPc/perovskite/$PC_{60}BM$/BCP/Ag. The *p-i-n* device based on **ZnPc-2** as HTLs measured a

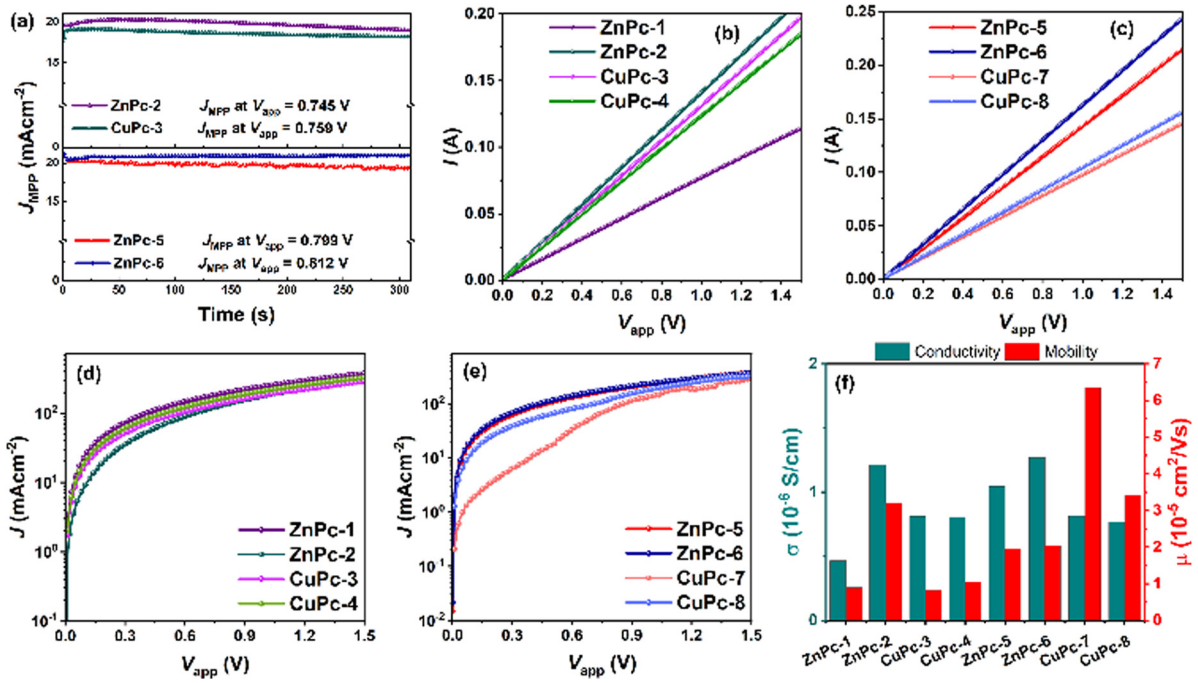

Fig. 7 (a) Steady-state photocurrent density for the continuous illumination at the maximum power point (MPP) for the devices in symmetric and asymmetric MPcs as HTLs, *I*–*V* curves for the conductivity measurement in the configuration of FTO/MPc/Ag for (b) symmetric MPcs and, (c) asymmetric MPcs, *J*–*V* curves for the hole mobility measurements in the configuration of FTO/PEDOT: PSS/MPc/Ag for (d) symmetric MPcs, and (e) asymmetric MPcs and (f) conductivity and mobility of each MPc summary.

PCE of 9.06% owing to V_{oc} of 901.87 mV, J_{sc} of 16.85 mA cm^{-2}, and FF of 59.59% followed by **ZnPc-6** with a 5.53% of PCE (Fig. S50 and Table S2, ESI†). However, the **ZnPc-5** in the *p-i-n* configuration yielded only a mere PCE of 3.88%. The observed low J_{sc} values from *p-i-n* devices could be attributed to the higher optical absorption in the whole visible range of these MPCs before the light reaching to the active perovskite layer, hindering the generation of photo-charges in the perovskite layer.

The charge transport abilities of each MPc were investigated by measuring their conductivity and mobility values. The electrical conductivity (σ) was extracted from the *I*–*V* (current–voltage) curve (Fig. 7b and c) of the device with the configuration of FTO/MPc/Ag along with the relation, $\sigma = (I/VA)d$, where d is the thickness of the HTM (avg. thickness of each MPc from the cross-sectional image of the hole-only device as shown in Fig. S51, ESI†) and A is the active area of the devices.[34] The space-charge-limited-current (SCLC) measurements were performed to evaluate the hole mobility (μ) of MPcs from semi-logarithmic $J_{0.5}$–V curves (Fig. 7d and e) of the hole-only device (FTO/PEDOT: PSS/MPc/Ag) along with the Mott–Gurney equation.[35]

$$J = 9\varepsilon\varepsilon_0\mu V_{app}{}^2/8L^3$$

The obtained values are summarized in Table S3 (ESI†). The highest conductivity was noted for fluorinated asymmetric **ZnPc-6** with 1.268 × 10^{-6} S cm^{-1}, which also exhibited the best PCE of PSCs. This was followed by **ZnPc-2** with a conductivity value of 1.21 × 10^{-6} S cm^{-1} followed by **ZnPc-5** with 1.05 × 10^{-6} S cm^{-1}; however, their PCE values are not correlated. Even though **CuPc-7** and **CuPc-8** show the highest mobility, they featured the lowest PCE. It is interesting to note that the conductivity and mobility values obtained from MPcs do not follow a similar trend of PCEs, suggesting that there is another reason apart from the symmetrical nature and the coordination metal in the MPc influences the PV performances. The lower values obtained in our synthesized MPcs compared with the already published diphenylamino substituted metallophthalocyanines[36] could be attributed to the effect of the alkoxy side chains influencing the molecular packing in the solid state of the HTMs, in a way that determined their ability to conduct charges and in the interaction with the perovskite layer.

To further understand photo-induced charge recombination in PSCs, we performed electrochemical impedance spectroscopy (EIS) under dark conditions for the PSCs with both symmetrical (**ZnPc-2** and **CuPc-3**) and asymmetrical (**ZnPc-5** and **ZnPc-6**) categories. The Nyquist plot (Fig. S52, ESI†) at different bias voltages from 0.85–1.05 V is fitted with the equivalent circuit of R_s + R_{rec}/CPE (dots and continuous lines represent raw and fitted curves, respectively), where R_s is the series resistance coming from the external circuit and R_{rec} is the recombination resistance of the PSC. A constant phase element related to carrier diffusion in selective layers and perovskite is assigned as CPE. At a given potential bias, the **ZnPc-6**-based PSC features a much higher R_{rec} (Fig. S53, ESI†), indicating that **ZnPc-6** leads to lower charge recombination and mitigated charge annihilation at the perovskite/HTL interface, which is consistent with the observed reduced V_{oc} losses in the PSC based on **ZnPc-6**.

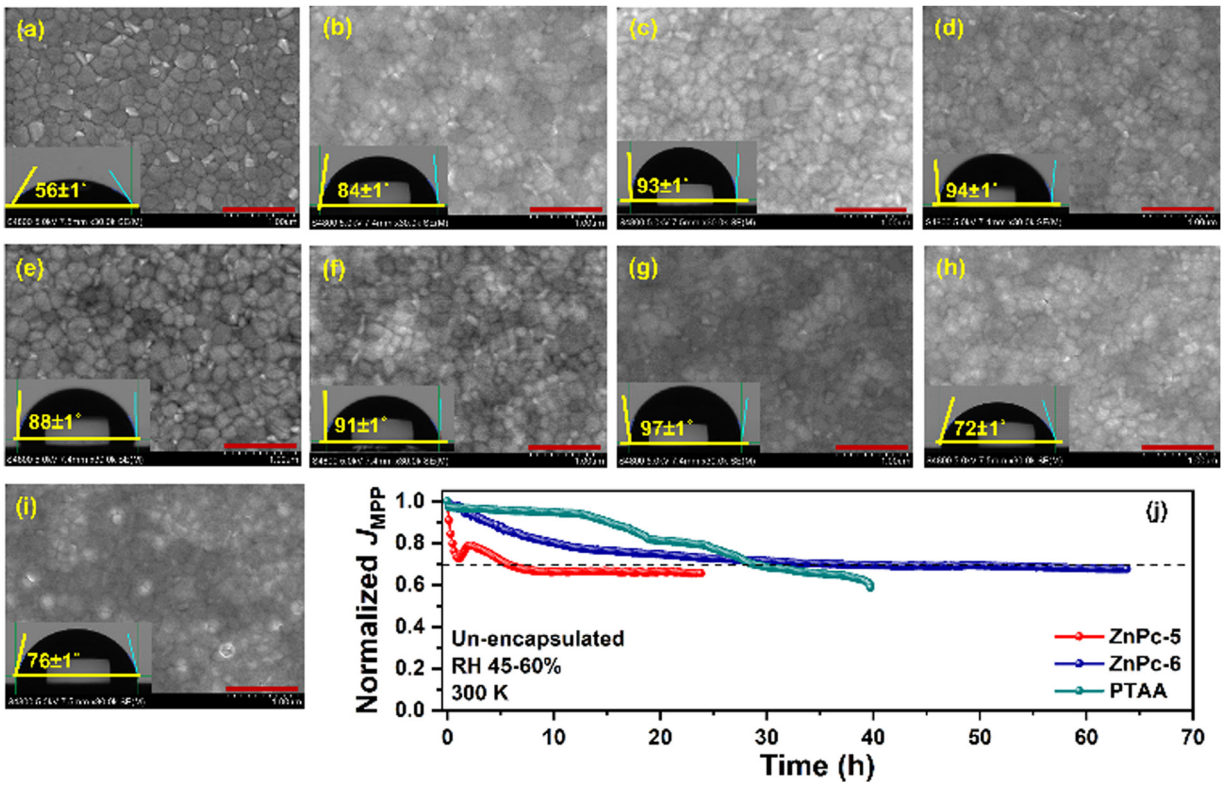

Fig. 8 Surface SEM image of (a) perovskite, (b) **ZnPc-1**, (c) **ZnPc-2**, (d) **CuPc-3**, (e) **CuPc-4**, (f) **ZnPc-5**, (g) **ZnPc-6**, (h) **CuPc-7**, and (i) **CuPc-8** deposited on perovskite. Inset: Corresponding water contact angle. The red lines represent the 1 μm scale bar, and (j) the normalized current density of continuous maximum power point (MPP) tracking for unencapsulated PSCs based on **ZnPc-5**, **ZnPc-6**, and pristine PTAA as HTMs under atmospheric conditions (RH 45-65%, 300 K).

The film-forming ability of any HTM is an important criterion to produce high-performance PSCs apart from the band alignment of the transport layer with the perovskite and their charge transportability. It is well known that non-covalent interactions between two or more phthalocyanine (Pcs) molecules cause their derivatives to aggregate, leading to their low solubility in the majority of solvents.[37,38] We observed that Cu-based Pcs give poor solubility and make clusters with time in chlorobenzene, a solvent used for device fabrication. Thus, the likely cause of the PV underperformance seen in some MPcs could be attributed to a lesser degree of solubility and the molecular accumulation that prevent the efficient energetic coupling and introduce recombination centers, thus responsible for the lower PCE measured for PSCs. The film-forming ability and the uniformity of MPcs on the perovskite were examined using scanning electron microscopy (SEM) and the surface image (Fig. 8a–i) and the corresponding water contact angle of different HTMs deposited on the perovskite layer is presented. The best performance featured from the **ZnPc-6** is ascribed to their uniform film-forming ability on the perovskite without any visible defects and pinholes, and this is further supported by a maximum water contact angle of 97 ± 1°. Further, **ZnPc-5**, **CuPc-3**, and **ZnPc-2** show uniform film coverage on the perovskite with the water contact angles of 91 ± 1°, 94 ± 1°, and 93 ± 1°, respectively. Different from this, an inhomogeneous surface with pinholes and aggregated molecular clusters could be observed from the **CuPc-7** and **CuPc-8** samples, which also results in a lower water contact angle owing to the higher wettability of the defective surfaces. Even though **CuPc-7** and **CuPc-8** produce significantly higher mobility, their reduced homogeneity on the perovskite layer induces a possible shunting pathway as indicated by their lower shunt resistance value and non-radiative charge recombination at the perovskite/HTM interface. This might be the plausible reason for the low PV performance noted from PSCs based on these two MPcs.

We also studied the long-term operational stability of the un-encapsulated devices (**ZnPc-5** and **ZnPc-6**) from the MPc series with reference PTAA device at their maximum power point (MPP) under ambient conditions (relative humidity of 45–60% and 300 K) under white LED light (Fig. 8j). While the PSCs based on **ZnPc-5** showed stabilized current density just below 70% of its initial value after rapid performance degradation at the early stage of the experiment, **ZnPc-6** performed better and showed a nearly linear response, holding around 70% of its initial current density for around 60 h. Particularly, the reference device based on pristine PTAA featured 70% of its original performance up to 30 h and speedy performance lost thereafter.

3. Experimental

Synthesis of phthalocyanines

All chemicals and solvents were purchased from Sigma Aldrich (Merck) and TCI and were used without further purification unless otherwise stated.

Lead Iodide (PbI_2, 99.9%) was procured from Tokyo Chemical Industry (TCI). Other chemicals for perovskite were purchased from Greatcell Solar and employed without further purification. PTAA (M_n = 5000–15000 by GPC) was obtained from Xi'an Polymer Light Technology Corp. [60]PCBM >99.5% and Bathocuproine (BCP) were purchased from Solenne BV and TCI, respectively. Tin (IV) oxide, 15% in H_2O colloidal dispersion, was obtained from Alfa Aesar. Chlorobenzene (CB, 99%), isopropanol (IPA, 99.9%), ethanol (EtOH, 99%), anhydrous dimethyl sulfoxide (DMSO, 99.8%), and *N*,*N*-dimethylformamide (DMF, 99.8%) were purchased from Acros Organics.

NMR spectra were recorded using a BRUKER AVANCE NEO 400 spectrometer. UV-vis spectra were recorded using a Perkin-Elmer Lambda 365 spectrophotometer. Fluorescence spectra were recorded using a HORIBA scientific SAS spectrophotometer. High-resolution mass spectra were obtained using a Bruker Microflex LRF20 matrix-assisted laser desorption/ionization-time of flight (MALDI-TOF) using dithranol as a matrix. IR spectra were recorded using a Nicolet Impact 400D spectrophotometer. Cyclic voltammetry was measured in a conventional three-electrode cell using a μ-AUTOLAB type III potentiostat/galvanostat at 298 K over DMF and deaerated sample solutions containing 0.10 M tetrabutylammonium hexafluorophosphate ($TBAPF_6$) as the supporting electrolyte. Platinum as the working electrode, $Ag/AgNO_3$ (0.01 M in benzonitrile) as the reference electrode, and platinum as the wire counter electrode were employed. Ferrocene/Ferrocenium redox couple was used as an internal standard for all measurements.

Synthesis of phthalonitrile 1

200 mg (0.79 mmol) of 4-iodophthalonitrile, 270.8 mg (1.18 mmol) of 4,4′-dimethoxydiphenylamine, 33.8 mg (0.04 mmol) of RuPhos Pd G4, 18.6 mg (0.04 mmol) of RuPhos and 518.2 mg (1.59 mmol) of Cs_2CO_3 were dissolved in 10 mL of deaerated toluene and heated to reflux in argon atmosphere for 24 hours. After cooling down to room temperature, H_2O was added to the crude product and it was extracted with DCM two times, dried with Na_2SO_4, filtered, and concentrated. It was purified by column chromatography (Hexane : AcOEt/8 : 2) obtaining 238 mg (85%) as a yellow powder. ^{1}H-NMR (400 MHz, $CDCl_3$): δ = 3.83 (s, 6*H*), 6.91–6.94 (m, 5*H*), 7.00–7.01 (d, *J* = 2.5 Hz, 1*H*), 7.09–7.13 (m, 4*H*), 7.41–7.43 (d, *J* = 8.9 Hz, 1*H*). ^{13}C-NMR (100 MHz, $CDCl_3$): δ = 55.7, 102.7, 115.7, 116.0, 116.7, 116.8, 119.2, 120.2, 128.2, 134.4, 137.1, 152.3, 158.3.

Synthesis of phthalonitrile 2

200 mg (0.79 mmol) of 4-iodophthalonitrile, 292 mg (1.18 mmol) of 3-fluoro-4-methoxy-*N*-(4-methoxyphenyl)aniline, 33.8 mg (0.04 mmol) of RuPhos Pd G4, 18.6 mg (0.04 mmol) of RuPhos and 518.2 mg (1.59 mmol) of Cs_2CO_3 were dissolved in 10 mL of deaerated toluene and heated to reflux in argon atmosphere for 24 hours. After cooling to room temperature, water was added and it was extracted two times with DCM, dried with Na_2SO_4, filtered, and concentrated under a vacuum. After purification by column chromatography (Hexane : AcOEt/75 : 25), 247 mg (84%) of **2** were obtained as a yellow powder. ^{1}H-NMR (400 MHz, $CDCl_3$): δ =3.83 (s, 3*H*), 3.91 (s, 3*H*), 6.90–6.95 (m, 6*H*), 7.04 (d, *J* = 2.5 Hz, 1*H*), 7.08–7.11 (d, *J* = 8.9 Hz, 2*H*), 7.44–7.46 (d, *J* = 8.8 Hz, 1*H*). ^{13}C-NMR (100 MHz, $CDCl_3$): δ = 55.7, 56.7, 103.6, 114.5, 114.6, 115.0, 115.2, 115.9, 115.9, 116.6, 117.0, 119.8, 120.8, 122.5, 122.5, 128.3, 134.5, 136.8, 137.3, 137.4, 146.6, 146.7, 151.7, 152.0, 154.2, 158.6.

Synthesis of ZnPc-1

35 mg (0.10 mmol) of **1** and 9 mg (0.05 mmol) of $Zn(OAc)_2$ in 200 μL of DMAE and one drop of DBN under an inert atmosphere were stirred at 130 °C for 16 hours. The purple mixture was cooled at room temperature, concentrated under vacuum, and purified by column chromatography (Hx : Dioxane/55 : 45) yielding 15 mg of **ZnPc-1** (43%) as a purple solid. ^{1}H-NMR (400 MHz, THF-d_8): (mixture of regioisomers), δ = 3.86 (d, *J* = 6.5 Hz, 24*H*), 7.03–6.97 (m, 16*H*), 7.37–7.28 (m, 16*H*), 7.60–7.54 (dd, *J* = 8.5, 1.8 Hz, 2*H*), 7.67–7.62 (dt, *J* = 8.4, 2.2 H, 2*H*), 8.70–8.67 (d, *J* = 12.5 Hz, 2*H*), 8.87–8.84 (dd, *J* = 11.0, 2.1 Hz 2*H*), 8.96–8.92 (dd, *J* = 8.4, 5.3 Hz, 2*H*), 9.10–9.07 (dd, *J* = 8.4, 3.4 Hz, 2*H*). HR-MALDI-TOF (dithranol): *m*/*z* for $C_{88}H_{68}N_{12}O_8Zn$: calcd 1484.4569 [M^+]; found, 1484.4632. UV-vis (DMF) λ_{max}/nm (log ε): 371 (4.77), 511 (4.14), 659 (4.47), 733 (5.13). FT-IR: ν_{max}/cm^{-1}: 3038, 2995, 2950, 2907, 2833, 1604, 1507, 1487, 1440, 1396, 1332, 1272, 1242, 1180, 1089, 1036, 883, 826, 756, 667, 585, 524, 434. Mp > 300 °C.

Synthesis of ZnPc-2

50 mg (0.13 mmol) of **2** and 12.28 mg (0.07 mmol) of $Zn(OAc)_2$ in 500 μL of DMAE and one drop of DBN under an inert atmosphere were stirred at 130 °C for 16 hours. The purple mixture was cooled at room temperature, concentrated under vacuum, and purified by column chromatography (Hx : Dioxane/55 : 45) yielding 14 mg of **ZnPc-2** (27%) as a purple solid. ^{1}H-NMR (400 MHz, THF-d_8): (mixture of regioisomers), δ = 3.86 (s, 12*H*), 3.92 (s, 12*H*), 7.40–6.9 (m, 32*H*), 7.65–7.62 (m, 4*H*), 9.05–8.74 (m, 8*H*). HR-MALDI-TOF (dithranol): *m*/*z* for $C_{88}H_{64}F_4N_{12}O_8Zn$: calcd. 1556.4192 [$M^+$]; found, 1556.4285. UV-vis (DMF) λ_{max}/nm (log ε): 372 (4.87), 495 (4.24), 653 (4.58), 726 (5.25). FT-IR: ν_{max}/cm^{-1}: 3058, 2999, 2952, 2908, 2835, 1606, 1507, 1488, 1398, 1333, 1263, 1243, 1181, 1089, 1032, 985, 828, 756, 664, 629, 584, 523, 437. Mp > 300 °C.

Synthesis of CuPc-3[24]

200 mg (0.56 mmol) of **1** and 38 mg (0.28 mmol) of $CuCl_2$ in 500 μL of DMAE and one drop of DBN under an inert atmosphere were stirred at 130 °C for 16 hours. The purple mixture was cooled at room temperature, concentrated under vacuum, and purified by column chromatography (Hx : Dioxane/55 : 45) and washed with MeOH, yielding 20 mg of **CuPc-3** (10%) as a purple solid. HR-MALDI-TOF (dithranol): *m*/*z* for $C_{88}H_{68}CuN_{12}O_8$: calcd. 1483.4573 [M^+]; found, 1483.4652. UV-vis (DMF) λ_{max}/nm (log ε): 343 (4.88), 501 (4.35), 671 (4.49), 749 (5.02). FT-IR: ν_{max}/cm^{-1} : 3059, 2995, 2929, 2832, 1605, 1506, 1404, 1338, 1272, 1241, 1179, 1094, 1035, 892, 826, 758, 589, 525, 424. Mp > 300 °C.

Synthesis of CuPc-4

100 mg (0.27 mmol) of **2** and 18 mg (0.13 mmol) of $CuCl_2$ in 500 μL of DMAE and one drop of DBN under an inert atmosphere were stirred at 130 °C for 16 hours. The purple mixture was cooled at room temperature, concentrated under vacuum, and purified by column chromatography ($CHCl_3$: MeOH/99 : 1) and washed with MeOH, yielding 10 mg of **CuPc-4** (10%) as a purple solid. HR-MALDI-TOF (dithranol): *m/z* for $C_{88}H_{64}CuF_4N_{12}O_8$: calcd 1555.4197 [$M^+$]; found, 1555.4241. UV-vis (DMF) λ_{max}/nm ($\log\varepsilon$): 346 (4.92), 498 (4.36), 666 (4.52), 740 (5.10). FT-IR: ν_{max}/cm^{-1}: 3059, 2998, 2932, 2834, 1607, 1506, 1404, 1339, 1263, 1243, 1181, 1093, 1032, 826, 758, 629, 524, 436. Mp > 300 °C.

Synthesis of ZnPc-5

90 mg (0.25 mmol) of **1** 186.63 mg (1.01 mmol) of 4-*tert*-butylphthalonitrile and 92.92 mg (0.51 mmol) of $Zn(OAc)_2$ in 750 μL of DMAE and two drops of DBN under inert atmosphere were stirred at 130 °C for 16 hours. The blue mixture was cooled at room temperature, concentrated under vacuum, and purified by column chromatography (Hx : Dioxane/75 : 25) yielding 34 mg of **ZnPc-5** (14%) as a blue solid. ^{1}H-NMR (400 MHz, THF-d_8): (mixture of regioisomers), δ = 1.80–1.77 (m, 27*H*) 3.89 (s, 6*H*), 7.08–7.04 (m, 4*H*), 7.43–7.39 (m, 4*H*), 7.73–7.71 (m, 1*H*), 8.30–8.20 (m, 3*H*), 8.96–8.92 (m, 1*H*), 9.21–9.27 (m, 1.5*H*), 9.40–9.32 (m, 3*H*), 9.54–9.50 (m, 2.5*H*). HR-MALDI-TOF (dithranol): *m/z* for $C_{58}H_{53}N_9O_2Zn$: calcd 971.3608 [M^+]; found, 971.3896. UV-vis (DMF) λ_{max}/nm ($\log\varepsilon$): 353 (4.71), 624 (4.41), 692 (5.14). FT-IR: ν_{max}/cm^{-1}: 3066, 2955, 2903, 2865, 2834, 1610, 1506, 1489, 1441, 1393, 1329, 1281, 1242, 1181, 1090, 1047, 922, 889, 829, 747, 693, 603, 576, 527, 445. Mp> 300 °C.

Synthesis of ZnPc-6

90 mg (0.24 mmol) of **2** 137.67 mg (0.75 mmol) of 4-*tert*-butylphthalonitrile and 88.45 mg (0.48 mmol) of $Zn(OAc)_2$ in 750 μL of DMAE and two drops of DBN under inert atmosphere were stirred at 130 °C for 16 hours. The blue mixture was cooled at room temperature, concentrated under vacuum, and purified by column chromatography (Hx : Dioxane/75 : 25) yielding 38 mg of **ZnPc-6** (16%) as a blue solid. ^{1}H-NMR (400 MHz, THF-d_8): (mixture of regioisomers), δ = 1.80–1.77 (m, 27*H*) 3.89 (br, 3*H*), 3.95 (br, 3*H*), 7.09–7.06 (m, 2*H*), 7.20–7.17 (m, 3*H*), 7.43–7.39 (m, 2*H*), 7.79–7.74 (m, 1*H*), 8.31–8.21 (m, 3*H*), 9.00–9.87 (m, 1*H*), 9.25–9.19 (m, 1.5*H*), 9.40–9.33 (m, 3*H*), 9.55–9.51 (m, 2.5*H*). HR-MALDI-TOF (dithranol): *m/z* for $C_{58}H_{52}FN_9O_2Zn$: calcd 989.3514 [M^+]; found, 989.3613. UV-vis (DMF) λ_{max}/nm ($\log\varepsilon$): 352 (4.90), 622 (4.60), 690(5.35). FT-IR: ν_{max}/cm^{-1}: 3069, 2955, 2904, 2865, 1608, 1506, 1489, 1441, 1392, 1330, 1282, 1256, 1243, 1181, 1090, 1047, 921, 894, 828, 746, 692, 604, 526, 444. Mp > 300 °C.

Synthesis of CuPc-7

100 mg (0.28 mmol) of **1**, 181.44 mg (0.99 mmol) of 4-*tert*-butylphthalonitrile and 75.66 mg (0.56 mmol) of $CuCl_2$ in 750 μL of DMAE and one drop of DBN under inert atmosphere were stirred at 130 °C for 16 hours. The blue mixture was cooled at room temperature, concentrated under vacuum, and purified by column chromatography ($CHCl_3$: THF/99.5 : 0.5) and washed with MeOH, yielding 21 mg of **CuPc-7** (8%) as a blue solid. HR-MALDI-TOF (dithranol): *m/z* for $C_{58}H_{53}CuN_9O_2$: calcd 970.3613 [M^+]; found, 970.3705. UV-vis (DMF) λ_{max}/nm ($\log\varepsilon$): 345 (4.86), 628 (4.49), 697 (5.14). FT-IR: ν_{max}/cm^{-1}: 3060, 2954, 2902, 2833, 1614, 1506, 1406, 1325, 1282, 1241, 1181, 1092, 1038, 930, 827, 749, 671, 575, 530. Mp > 300 °C.

Synthesis of CuPc-8

100 mg (0.27 mmol) of **2**, 173 mg (0.94 mmol) of 4-*tert*-butylphthalonitrile and 72 mg (0.54 mmol) of $CuCl_2$ in 750 μL of DMAE and one drop of DBN under an inert atmosphere were stirred at 130 °C for 16 hours. The blue mixture was cooled at room temperature, concentrated under vacuum and purified by column chromatography ($CHCl_3$: MeOH/99.5 : 0.5), and washed with MeOH, yielding 22 mg of **CuPc-8** (8%) as a blue solid. HR-MALDI-TOF (dithranol): *m/z* for $C_{58}H_{52}CuFN_9O_2$: calcd 988.3519 [M^+]; found, 988.3596. UV-vis (DMF) λ_{max}/nm ($\log\varepsilon$): 346 (4.89), 626 (4.52), 694 (5.19). FT-IR: ν_{max}/cm^{-1}: 3068, 2956, 2903, 2866, 1611, 1507, 1407, 1326, 1258, 1243, 1153, 1092, 1034, 930, 829, 749, 694, 530, 435. Mp > 300 °C.

Device fabrication

n–i–p device. Following successive sonication with Hellmanex II (2 vol% in deionized water), deionized water, ethanol, acetone, and isopropanol, the laser-etched FTO-coated glass substrates (TEC15) were dried using compressed airflow. Before usage, the substrates underwent further treatment with UV-ozone for 30 minutes. Spray pyrolysis at 500 °C with 1/19 mL of titanium (IV) diisopropoxide bis(acetylacetonate) precursor solution (75% in 2-propanol) in pure ethanol was used to produce a compact TiO_2 blocking layer onto FTO substrates. The electron transport layer (ETL) was fabricated using colloidal SnO_2 2.67% water solution *via* spin coating at 5000 rpm for 30 s, followed by annealing at 180 °C for 1 h in air. Once cooled down to room temperature, the samples were transferred to the Argon-filled glovebox (H_2O level: <1 ppm and O_2 level: <10 ppm). $Cs_{0.1}(FA_{0.9}MA_{0.1})_{0.9}Pb(I_{0.9}Br_{0.1})_3$ perovskite precursor solution was prepared according to the previous report.[29] The perovskite precursor solution was spin-coated on the as-prepared SnO_2 ETL in an antisolvent-assisted two-step spin-coating program set at 1000 rpm and 6000 rpm for 10 and 30 s followed by annealing at 100 °C for 1 h to induce perovskite crystallization. 10 mM of each MPc-HTM in chlorobenzene was spin-coated on perovskite at 4000 rpm for 20 s at room temperature. Pristine PTAA (10 mg ml^{-1} in toluene) was spin-coated at 3000 rpm for 35 s to construct the reference device. ~70 nm gold electrode was evaporated (<1 Å s^{-1}) by thermal evaporation under low vacuum conditions below 10^{-6} Torr as a final electrode.

***p-i-n* device.** The device was fabricated according to the previous report with modification noted herein.[39] 2 mM of each MPc-HTM in chlorobenzene was spin-coated atop the cleaned FTO substrates at 3000 rpm for 30 s. $Cs_{0.1}(FA_{0.9}MA_{0.1})_{0.9}Pb(I_{0.9}Br_{0.1})_3$ perovskite film was achieved as described previously. The PCBM solution of 15 mg ml^{-1} in chlorobenzene

was spin-coated at room temperature on perovskite film at 1000 rpm (500 rpm s^{-1}) for 20 s followed by annealing at 90 °C for 10 min. A thin layer of BCP (0.5 mg mL^{-1} in IPA) was deposited atop PCBM by spin coating at 5000 rpm for 40 s. The device fabrication was completed by evaporating Ag (100 nm, <1 Å s^{-1}) in a thermal evaporator under low vacuum conditions (below 10^{-6} Torr).

Thin-film characterization and device characterization

To quantify absorption spectra, a Varian Cary 50 UV-vis spectrophotometer was used. We utilized field emission scanning electron microscopy to assess the surface microstructure (Hitachi S-4800). The current–density (*J–V*) curves were recorded using a Keithley 2400 source meter with a solar simulator (Newport, ORIEL AAA solar simulator) under irradiation of 100 mW cm^{-2} (AM1.5). An NREL-certified calibrated monocrystalline silicon solar cell was used for the calibration. The generated photocurrent was recorded at a scan rate of 100 mV s^{-1} (pre-sweep delay: 10 s) and a 0.09 cm^2 black metal mask was used as an active area of the devices. The external quantum efficiency (EQE) spectra were carried out using a 150 W Xenon lamp along with a Bentham PVE300 motorized 1/4 m monochromator as the light source. Electrochemical impedance spectroscopy (EIS) was performed using a BioLogic SP-300 impedance analyser in the frequency range of 2 MHz–1 Hz under the ac signal in a faradaic chamber, and the resulting data were fitted with EC-Lab software.

4. Conclusions

We have synthesized eight different arylamino MPcs, to provide a molecular guideline for the designing of MPcs as hole-selective materials for the fabrication of perovskite solar cells. We unravel the influence of the number of aryl amino groups, the presence of fluorine atoms, the central metal, and the symmetry of the molecule on photovoltaic performance. The incorporation of the fluorine atom into arylamino-substituted MPcs is an effective strategy for the performance and stability enhancement in perovskite solar cells. We noted that the PCE not only depends on the symmetrical nature of the side chain of the MPc but also the metal species attached to it. A higher conductivity is found for asymmetric fluorinated **ZnPc-6** and it also translates into high PV performance suggesting the variation in the energy level of the perovskite impacts the PV performances apart from the symmetrical nature and the coordination metal in MPc.

Author contributions

A. H. and J. O. carried out the synthesis and characterization of all the compounds. N. H. H and A. H. S. K. performed the experiments, fabricated the devices, and analysed the data. A. H., J. O., and N. H. H prepared the initial draft. S. K., J. O., S. A., and A. S. S. supervised, drafted, and directed the research. All authors contributed to the draft and prepared the final version.

Conflicts of interest

There are no conflicts to declare.

Acknowledgements

This work received funding from the European Union H2020 Programme under a European Research Council Consolidator grant [MOLEMAT, 726360]. Support from the Spanish Ministry of Science and Innovation (PID2019-111774RB-100/AEI/10.13039/501100011033 and INTERACTION {PID2021-129085OB-I00}) is also acknowledged. We want to thank the European Regional Development Fund "A way to make Europe" and the Spanish Ministerio de Ciencia e Innovación/Agencia Estatal de Investigación (PID2020-117855 RB-I00 to Á.S.-S) and the Generalitat Valenciana (CIPROM/2021/059 and MFA/2022/028 to Á. S.-S.) for funding.

References

1 A. Kojima, K. Teshima, Y. Shirai and T. Miyasaka, *J. Am. Chem. Soc.*, 2009, **131**, 6050–6051; L. Calió, S. Kazim, M. Grätzel and S. Ahmad, *Angew. Chem., Int. Ed.*, 2016, **55**, 14522–14545.
2 **https://www.nrel.gov/pv/cell-efficiency.html** (accessed 12/03/2023).
3 C. S. Ponseca, T. J. Savenije, M. Abdellah, K. Zheng, A. Yartsev, T. Pascher, T. Harlang, P. Chabera, T. Pullerits, A. Stepanov, J.-P. Wolf and V. Sundström, *J. Am. Chem. Soc.*, 2014, **136**, 5189–5192.
4 S. D. Stranks, G. E. Eperon, G. Grancini, C. Menelaou, M. J. P. Alcocer, T. Leijtens, L. M. Herz, A. Petrozza and H. J. Snaith, *Science*, 2013, **342**, 341–344.
5 W.-J. Yin, T. Shi and Y. Yan, *Adv. Mater.*, 2014, **26**, 4653.
6 M. Cai, Y. Wu, H. Chen, X. Yang, Y. Qiang and L. Han, *Adv. Sci.*, 2017, **4**, 1600269.
7 G.-W. Kim, H. Choi, M. Kim, J. Lee, S. Y. Son and T. Park, *Adv. Energy Mater.*, 2020, **10**, 1903403.
8 A. Krishna and A. C. Grimsdale, *J. Mater. Chem. A*, 2017, **5**, 16446.
9 G. Ren, W. Han, Y. Deng, W. Wu, Z. Li, J. Guo, H. Bao, C. Liu and W. Guo, *J. Mater. Chem. A*, 2021, **9**, 4589–4625.
10 H. D. Pham, T. C.-J. Yang, S. M. Jain, G. J. Wilson and P. Sonar, *Adv. Energy Mater.*, 2020, **10**, 1903326.
11 E. Kasparavicius, A. Magomedov, T. Malinauskas and V. Getautis, *Chem. – Eur. J.*, 2018, **24**, 9910.
12 X. Yin, Z. Song, Z. Li and W. Tang, *Energy Environ. Sci.*, 2020, **13**, 4057–4086.
13 G. Bottari, G. de la Torre, D. M. Guldi and T. Torres, *Coord. Chem. Rev.*, 2021, **428**, 213605.
14 (*a*) D. Molina, J. F. Berna and A. Sastre-Santos, *J. Mater. Chem. C*, 2023, DOI: **10.1039/D2TC04441B**; (*b*) M. Urbani,

G. de la Torre, M. K. Nazeeruddin and T. Torres, *Chem. Soc. Rev.*, 2019, **48**, 2738–2766.
15 A. M. Schmidt and M. J. F. Calvete, *Molecules*, 2021, **26**, 1.
16 D. Molina, M. A. Ruiz-Preciado, F. Sadegh, M. J. Álvaro-Martins, M. Grätzel, A. Hagfeld and Á. Sastre-Santos, *J. Porphyrins Phthalocyanines*, 2019, **23**, 546–553.
17 D. Molina, M. A. Ruiz-Preciado, B. Carlsen, F. T. Eickemeyer, B. Yang, N. Flores-Díaz, M. J. Álvaro-Martins, K. Nonomura, A. Hagfeldt and Á. Sastre-Santos, *ChemPhotoChem*, 2020, **4**, 307–314.
18 M. Pegu, D. Molina, M. J. Álvaro-Martins, M. Castillo, L. Ferrer, P. Huang, S. Kazim, Á. Sastre-Santos and S. Ahmad, *J. Mater. Chem. C*, 2022, **10**, 11975–11982.
19 L. Caliò, J. Follana-Berná, S. Kazim, M. Madsen, H. G. Rubahn, Á. Sastre-Santos and S. Ahmad, *Sustainable Energy Fuels*, 2017, **1**, 2071–2077.
20 Z. Yu, L. Wang, X. Mu, C. C. Chen, Y. Wu, J. Cao and Y. Tang, *Angew. Chem., Int. Ed.*, 2021, **60**, 6294.
21 M. M. H. Desoky, M. Bonomo, R. Buscaino, A. Fin, G. Viscardi, C. Barolo and P. Quagliotto, *Energies*, 2021, **14**, 2279.
22 K. T. Cho, K. Rakstys, M. Cavazzini, S. Orlandi, G. Pozzi and M. K. Nazeeruddin, *Nano Energy*, 2016, **30**, 853.
23 G. Sfyri, N. Vamshikrishna, C. V. Kumar, L. Giribabu and P. Lianos, *Sol. Energy*, 2016, **140**, 60.
24 Y. Feng, Q. Hu, E. Rezaee, M. Li, Z. X. Xu, A. Lorenzoni, F. Mercuri and M. Muccini, *Adv. Energy Mater.*, 2019, **9**, 1.
25 N. Klipfel, J. Xia, P. Čulík, S. Orlandi, M. Cavazzini, N. Shibayama, H. Kanda, C. Igci, W. Li, Y.-B. Cheng, V. Jankauskas, K. Genevicius, A. M. Asiri, C. Momblona, K. Rakstys, G. Pozzi and M. K. Nazeeruddin, *Mater. Today Energy*, 2022, **29**, 101110.
26 P. Huang, A. Hernández, S. Kazim, J. Ortiz, Á. Sastre-Santos and S. Ahmad, *Sustainable Energy Fuels*, 2020, **4**, 6188–6195.
27 P. Huang, A. Hernández, S. Kazim, J. Follana-Berná, J. Ortiz, L. Lezama, Á. Sastre-Santos and S. Ahmad, *ACS Appl. Energy Mater.*, 2021, **4**(9), 10124–10135.
28 E. Oleiki, S. Javaid and G. Lee, *Nanoscale Adv.*, 2022, **4**, 5070–5076.
29 (*a*) J. Zhang, H. Lu, Y. Xu, C. Zhong, K. Chen, R. Tang, P. Zhang, F. Wu and L. Zhu, *J. Mater. Chem. C*, 2022, **10**, 14668–14674; (*b*) T. Qin, F. Wu, D. Ma, Y. Mu, X. Chen, Z. Yang, L. Zhu, Y. Zhang, J. Zhao and Z. Chi, *ACS Mater. Lett.*, 2020, **2**, 1093–1100.
30 N. H. Hemasiri, S. Kazim and S. Ahmad, *J. Mater. Chem. C*, 2021, **9**, 9865–9873.
31 I. Gelmetti, N. F. Montcada, A. P. Rodríguez, E. Barrena, C. Ocal, I. G. Benito, A. M. Ontoria, N. Martín, A. V. Ferran and E. Palomares, *Energy Environ. Sci.*, 2019, **12**, 1309–1316.
32 C. M. Wolff, F. Zu, A. Paulke, L. P. Toro, N. Koch and D. Neher, *Adv. Mater.*, 2017, **29**, 1700159.
33 N. Klipfel, J. Xia, P. Culík, S. Orlandi, M. Cavazzini, N. Shibayama, H. Kanda, C. Igci, W. Li, Y. B. Cheng, V. Jankauskas, K. Genevicius, A. M. Asiri, C. Momblona, K. Rakstys, G. Pozzi and M. K. Nazeeruddin, *Mater*, 2022, **29**, 101110.
34 Y. Cao, Y. Li, T. Morrissey, B. Lam, B. O. Patrick, D. J. Dvorak, Z. Xia, T. L. Kelly and C. P. Berlinguette, *Energy Environ. Sci.*, 2019, **12**, 3502–3507.
35 (*a*) T. Niu, W. Zhu, Y. Zhang, Q. Xue, X. Jiao, Z. Wang, Y. M. Xie, P. Li, R. Chen, F. Huang, Y. Li, H. L. Yip and Y. Cao, *Joule*, 2021, **5**, 249–269; (*b*) N. H. Hemasiri, L. Caliò, M. Pegu, S. Kazim and S. Ahmad, *Sol. RRL*, 2022, **6**, 2100793.
36 N. Klipfel, J. Xia, P. Culík, S. Orlandi, M. Cavazzini, N. Shibayama, H. Kanda, C. Igci, W. Li, Y.-B. Cheng, V. Jankauskas, K. Genevicius, A. M. Asiri, C. Momblona, K. Rakstys, G. Pozzi and M. K. Nazeeruddin, *Mater. Today Energy*, 2022, **29**, 101110.
37 D. Erzunov, T. Tikhomirova, A. Botnar, S. Znoyko, I. Abramov, V. Mayzlish, Y. Marfin and A. Vashurin, *J. Therm. Anal. Calorim.*, 2020, **142**, 1807–1816.
38 A. W. Snow, *The porphyrin handbook*, 2003, 129–176.
39 H. Dhifaoui, N. H. Hemasiri, W. Aloui, A. Bouazizi, S. Kazim and S. Ahmad, *Adv. Mater. Interfaces*, 2021, **8**, 2101002.